Electronic Supplementary Material (ESI) for Nanoscale.

Supporting Materials

Moving dynamics of a nanorobot with three DNA legs on nanopore-based tracks

Li-Zhen Sun*, Yao-Jun Ying

Department of Applied Physics, Zhejiang University of Technology, Hangzhou 310023, China

*Corresponding author:

E-mails: sunlizhen@zjut.edu.cn

S1. The force-field of the coarse-grained model

In our simulations, the DNA robot is formed by one nanoparticle and three single-stranded DNA (ssDNA) chains. The nanoparticle is represented by a large bead NP, while each ssDNA chain is a coarse-grained (CG) representation of polythymine with 16 nucleotides. Specifically, the atomic groups phosphate, sugar, and base thymine in each nucleotide are represented by beads P, S, and B, respectively. To determine the conformation of the DNA robot, we incorporate five energy functions into our CG model: the volume excluded interaction (U_{lj}), the virtual bond interaction (U_b), the bond-bond angle potential (U_a), the dihedral potential (U_d), and the bead P-bead P electrostatic interaction (U_e).

The volume excluded interaction U_{lj} between the non-bonded beads are described by the Lennard-Jones (LJ) potential:

$$U_{lj} = \begin{cases} \varepsilon_{lj}[(\frac{\sigma}{r})^{12} - 2(\frac{\sigma}{r})^{6}] - U_{cut}, \text{ for } r < r_{cut} \\ 0, \quad \text{otherwise} \end{cases} \tag{S1}$$

Here ε_{lj} denotes the potential strength and r is the distance between two beads. For the volume excluded interactions between the beads of the DNA robot, the LJ strength ε_{lj} = 0.35 [S1], while for the interactions between robot beads and non-robot beads (wall and pore) beads, the LJ strength ε_{lj} = 1 [S2]. The equilibrium distance σ equals the sum of two bead radii. The cutoff potential $U_{cut} = \varepsilon_{lj}[(\frac{\sigma}{r_{cut}})^{12} - 2(\frac{\sigma}{r_{cut}})^{6}]$ makes the LJ potential continuous at the cutoff distance r_{cut} (= σ).

For each ssDNA chain, the neighbouring beads are connected *via* three types of the virtual bonds, bond P-S, bond S-P, and bond B-S. Moreover, there is another virtual bond B-NP to connect the bead B in the terminal nucleotide at 3' end of the ssDNA with the bead NP (nanoparticle). The virtual bond interaction U_b is given by:

$$U_b = k_b(b - b_0)^2 \tag{S2}$$

Here b represents the distance between two bonded beads. Parameters k_b and b_0 are the

stretching strength and equilibrium length of the bond.

These four types of virtual bonds can form five types of bond angles: P-S-P, S-P-S, P-S-B, B-S-P, and S-NP-S. The first four angles are formed by the adjacent bonds of one ssDNA chain, and the last one is used to describe the relevant positions of the bead NP and the terminal beads S in two different ssDNA chains. The bond-bond angle potential U_a is expressed by:

$$U_a = k_a(\theta - \theta_0)^2 \tag{S3}$$

Here θ represents the bond angle. k_a and θ_0 denote the angle strength and equilibrium angle between two adjacent bonds.

There are no base pairs between the bases of the polythymines. As the unpaired bases-involved dihedral angles have weak effects on the ssDNA conformations [S3], only two dihedral angles P-S-P-S and S-P-S-P in the ssDNA backbone are taken into account in the current CG model. The dihedral potential U_d reads as follow [S4]:

$$U_d = \sum_{n=1}^{4} k_n[1 + \cos(n\lambda - \lambda_n)] \tag{S4}$$

Here λ represents the dihedral angle. λ_n and k_n (n=1, 2, 3, 4) are the four local minimums of the dihedral angles and corresponding dihedral angle strengths.

For the bond-involved interaction of each ssDNA chain, the potential parameters in Eqs. (S2)-(S4) are derived from the Boltzmann inversion of the correspondingly structural normalized probability distributions, which can be statistically obtained from the experimentally measured ssDNA structures; while for the bead NP-involve interactions, the parameters are artificially fixed to maintain the connections between the bead NP and the ssDNA chains. The values of the parameters can be found in the table S2.

In the DNA robot-membrane system, only bead P is assumed to carry a negative

charge, while other beads are treated neutral. The system is simulated in 0.1mol/L NaCl solution. The electrostatic interaction U_e between the charged beads is estimated by Manning counterion condensation model [S5]:

$$U_e = \frac{Q^2 l_B}{r}\exp(-\kappa r) \tag{S5}$$

Here l_B [$= e^2/(4\pi\varepsilon_0\varepsilon_W k_B T)$] is the Bjerrum length with ε_0 as the dielectric constant of vacuum, ε_W (= 78.5 at the room temperature) as the relative dielectric constant of solvent, k_B as the Boltzmann constant, and T as the temperature. The effective charge constant $Q = C_s/l_B$ with C_s (=4.4Å [S6]) as the charge spacing on the ssDNA backbone. The exponent part reflects the screening effect induced by the background ions and the Debye screening length κ is given by:

$$\kappa = \sqrt{4\pi l_B \sum (Z_j^2 c_j)} \tag{S6}$$

Here the subscript j represents the ion species (Na^+ and Cl^- in this study). Z_j and c_j represent the valence and background concentration of the ion species j.

S2. Snapshots before the state F2 for the selected jumping event

From the selected jumping event shown in Fig. 3(D) in the main paper, it is observed that when leg2 finds pore II (at state F2), leg1 has already left pore I. To provide a complete view of this jumping event, we supplementally present the moving process of the nanorobot before state F2 in Fig. S1. After the state F1, in which leg1 finds pore I, several nucleotides of leg1 can enter this pore (as seen in the snapshot at 11.8 ns). However, due to the entropic barrier generated during the entering process, leg1 retreats outside of the pore (as seen in the snapshot at 32.4 ns) and then moves near the pore entry (as seen in the snapshot at 37.4 ns). Subsequently, although leg1 leaves pore I, leg2 slowly approaches pore II (as seen in the snapshots at 44.0 ns and 53.1 ns). Then, leg2 gets close to pore II at 55.8 ns, and finally, state F2 occurs when a non-terminal nucleotide enters the pore.

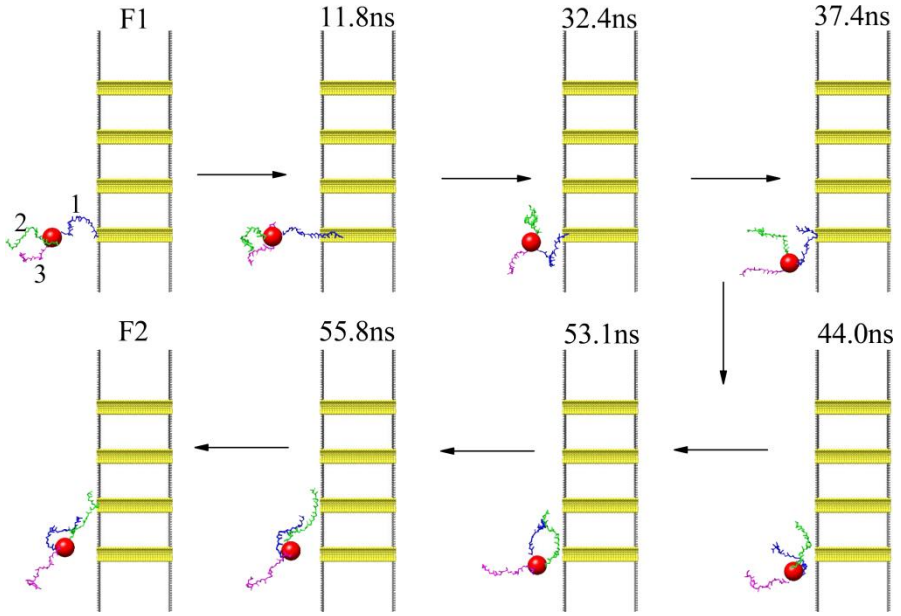

Fig. S1. Snapshots of the nanorobot during the step I-II (from state F1 to state F2) for the jumping event presented in Fig. 3(D) of the main paper. Leg1, leg2, and leg3 are highlighted in blue, green, and magenta, respectively.

S3. Another type of jumping mode

In the jumping events of the nanorobot moving on the nanopore-based track, the jumping behavior can be observed in the step II-III (see Fig. 3 presented in the main paper) or step III-IV (see Fig. S2). Fig. S2(A) depicts the trajectory of the nanoparticle during the jumping event, where the jumping behavior occurs in the step III-IV. Initially, the moving of the nanorobot follows the walking mode pattern, sequentially going through states F2, E2, and F3 (see Fig. S2B). However, after state F3, leg3 directly finds pore IV (state F4) without entering pore III, resulting in the absence of state E3 in the step III-IV.

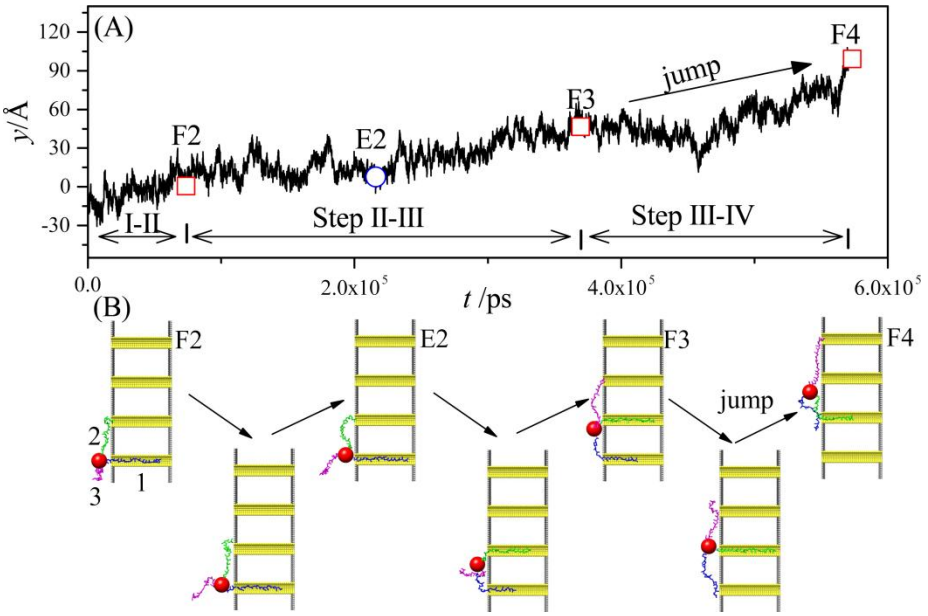

Fig. S2. Time-evolutional trace of the nanoparicle (A) and Corresponding snapshots of the nanorobot states (B) for the jumping mode with the jumping behavior observed in the step III-IV. Leg1, leg2, and leg3 are colored in blue, green, and magenta, respectively.

S4. Nanorobot moving on the nanopores with high charge densities

In the study of the nanorobot moving on the nanopore-based track, a natural question arises: How long can this nanorobot go? Due to the limitations of our computational resources, direct simulations of the nanorobot moving over a very long nanopore-based track are challenging. To address this, we adopt an alternative approach by increasing the charge densities of the nanopores in the four-nanopore platform. This allows us to mimic the nanopores where the nanorobot would be positioned after moving a long distance. In Fig. S3(A), we present the 2D electrostatic potentials φ near the platform surface with the bead charge of the pore I $q_0 = 0.5e$ and $2.5e$. The pore-pore distance and charge gradient are fixed as $D_p = 60$Å and $\Delta q = 0.25e$, respectively.

Compared to the case with a small q_0, a larger q_0 can hinder the moving of the nanorobot for two primary reasons. Firstly, as depicted in Fig. S3(B), a pore with higher charge density generates a larger electrostatic potential, creating a deeper

potential well for the robot legs. Consequently, it becomes more challenging for the nanorobot to move forward. Secondly, the pores with higher charges attract more counterions from the solution, leading to stronger screening effects. As a result, the potential gradient along the nanopore-based track decreases with an increase in q_0, as shown in Fig. S3(C).

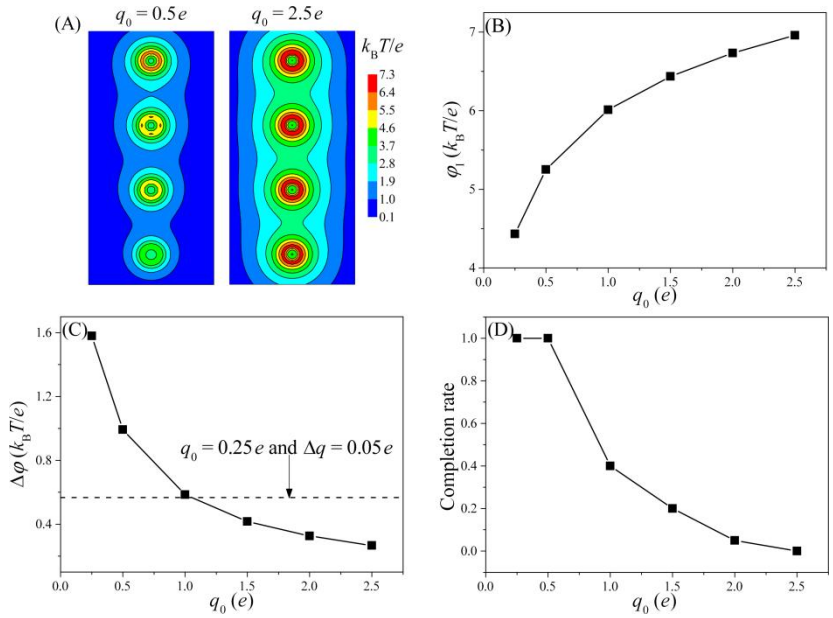

Fig. S3. (A) The 2D electrostatic potentials φ at the y-z plane of x = -2Å for the cases of q_0 = 0.5e (left panel) and q_0 = 2.5e (right panel). (B and C) The q_0-dependent electrostatic potential φ_I at the center of the entry of the pore I (B) and the potential difference $\Delta\varphi$ between the pore IV and pore I (C). (D) The probability of the successful moving for the nanorobot on the nanopore-based track with different q_0. The data presented in this figure are obtained from the simulation parameters as D_p = 60Å, Δq = 0.25e, ΔV =0, and N = 16nts.

In Fig. S3(D), we present the completion rate of a nanorobot with 16nts-long legs as it moves along nanopore-based tracks with different values of q_0. A complete moving event of the nanorobot is defined as the nanorobot successfully finding pore IV (state F4) within 10^7 simulation steps (approximately 6.2 ms). We conduct 20 independent samples for each type of track with a fixed q_0. Our observations reveal that at small q_0 values ($\leq$ 0.5e), the nanorobot can consistently complete the moving process within

the specified time. However, as the charge density increases, the completion rate of the nanorobot moving decreases. At $q_0 = 2.5e$ (i.e., the charge density of pore I is 0.36 e/Å^2), no complete moving events are observed. This indicates that the nanorobot cannot continue to move along the track when the charge density of the pore increases to 0.36 e/Å^2.

Table S1. Parameters in the CG model of the DNA robot

bead type	radius (Å)	mass (Da)	charge
NP	10.0	240	0
P	2.0[a]	95	$-Qe$[b]
S	2.9[a]	76	0
B	2.7[a]	120	0
wall bead	1.5	--[b]	0
pore bead	1.5	--[b]	0

[a] The radii of the beads P, S, and B come from the reference [S7].

[b] Q represents the manning constant (see Eq. (S5)).

[c] As the wall and pore beads are stationary, their masses are excluded from the simulations.

Table S2. Parameters in the potential field

		P-S	S-P	S-B	B-NP	
bond potential [a]	k_b	4.5	19.5	18.0	50.0	
	b_0	4.11	3.8	4.3	15.0	
		P-S-P	S-P-S	P-S-B	B-S-P	B-NP-B
angle potential [b]	k_a	4.0	5.8	10.6	11.8	20.0
	θ_0	1.91	1.57	1.66	2.23	2.09
			P-S-P-S			
		k_1	k_2	k_3	k_4	
		1.60	0.85	0.33	0.23	
		λ_1	λ_2	λ_3	λ_4	
dihedral angle		0.08	-0.87	-0.52	-0.66	
potential [b]			S-P-S-P			
		k_1	k_2	k_3	k_4	
		1.37	-0.70	0.38	-0.28	
		λ_1	λ_2	λ_3	λ_4	
		0.04	0.11	-1.28	0.35	

[a] the units of the parameters k_b and b_0 are $k_BT/Å^2$ and Å.

[b] the units of k_a and k_n are k_BT/rad^2, and the units of θ_0 and λ_n are radian.

Table S3. The simulation data of the moving dynamics for the DNA robot under various pore-pore distances D_p[a]

D_p(Å)[b]	P_L	p_w	p_j	v(×10^{-4}Å/ps)	τ_a(×10^{5}ps)	τ_f(×10^{5}ps)
48	0.205±0.027	0.05	0.95	2.25±0.21	2.00±0.22	0.82±0.16
54	0.185±0.025	0.31	0.69	2.47±0.20	1.87±0.19	1.40±0.19
60	0.191±0.025	0.75	0.25	1.61±0.09	3.26±0.29	2.73±0.17
72	0.198±0.028	0.99	0.01	1.57±0.09	4.71±0.44	3.59±0.17
84	0.149±0.026	0.98	0.02	0.88±0.05	13.67±1.09	4.97±0.29
96	0.135±0.037	0.975	0.025	0.37±0.03	43.05±4.64	7.20±0.74

[a] The charge gradient and the external voltage are fixed as $\Delta q = 0.25e$ and $\Delta V = 0$ in simulations.

[b] The first column to the seventh column show the pore-pore distance D_p, the successful landing probability of the DNA robot P_L, the probabilities of the walking mode p_w and the jumping mode p_j, the moving velocity v, the conformational adjustment duration τ_a, and the forward-moving duration τ_f.

Table S4. The simulation data of the moving dynamics for the DNA robot under various charge gradients Δq[a]

$\Delta q(e)$	P_L	p_w	p_j	$v(\times 10^{-4}$Å/ps)	$\tau_a(\times 10^5$ps)	$\tau_f(\times 10^5$ps)
0.05	0.109±0.016	0.90	0.10	0.77±0.08	10.51±1.47	3.38±0.28
0.10	0.127±0.023	0.90	0.10	0.96±0.06	6.97±0.60	3.69±0.22
0.15	0.137±0.021	0.85	0.15	1.31±0.08	4.47±0.45	3.24±0.18
0.25	0.191±0.025	0.75	0.25	1.61±0.09	3.26±0.29	2.73±0.17
0.35	0.235±0.032	0.79	0.21	1.94±0.10	2.67±0.20	2.46±0.13
0.45	0.229±0.039	0.66	0.34	2.12±0.13	2.37±0.19	2.14±0.16

[a] The pore-pore distance and the external voltage are fixed as $D_p = 60$Å and $\Delta V = 0$ in simulations.

Table S5. The simulation data of the moving dynamics for the DNA robot under various external voltage ΔV[a]

$\Delta V(V_0)$[b]	P_L	p_w	p_j	$v(\times 10^{-4}$Å/ps)	$\tau_a(\times 10^5$ps)	$\tau_f(\times 10^5$ps)
0	0.191±0.025	0.75	0.25	1.61±0.09	3.26±0.29	2.73±0.17
1	0.215±0.027	0.92	0.08	1.71±0.10	2.60±0.23	3.22±0.20
3	0.279±0.031	0.95	0.05	1.56±0.08	2.27±0.24	4.38±0.28
5	0.303±0.031	0.99	0.01	1.55±0.07	1.43±0.13	5.48±0.29
7	0.398±0.035	0.99	0.01	1.27±0.08	1.70±0.28	6.84±0.50
9	0.450±0.049	0.96	0.04	0.93±0.08	3.33±0.82	8.39±0.78
10	0.437±0.043	0.96	0.04	0.67±0.07	6.06±1.12	9.97±1.21

[a] The pore-pore distance and the charge gradient are fixed as $D_p = 60$Å and $\Delta q = 0.25e$ in simulations.

[b] The unit of the external voltage is $V_0 = 25.8$mV.

Table S6. The simulation data of the moving dynamics for the DNA robot under various leg length N[a].

N(nts)	P_L	p_w	p_j	v(×10^{-4}Å/ps)	τ_a(×10^{5}ps)	τ_f(×10^{5}ps)	D (Å)
12	0.229±0.029	0.88	0.12	1.78±0.11	4.67±0.37	1.50±0.07	109.8±1.2
14	0.202±0.026	0.9	0.1	1.95±0.11	3.36±0.27	2.05±0.11	105.5±1.3
16	0.191±0.025	0.75	0.25	1.61±0.09	3.26±0.29	2.73±0.17	96.6±1.4
18	0.139±0.022	0.62	0.38	1.54±0.10	2.75±0.25	3.15±0.26	90.8±1.9
20	0.116±0.017	0.44	0.56	1.53±0.09	2.54±0.29	3.17±0.28	87.6±2.3

[a] The pore-pore distance, charge gradient, and the external voltage are fixed as D_p = 60Å, $\Delta q = 0.25e$, and $\Delta V = 0$ in simulations.

References

[S1] Y. Z. Shi, L. Jin, C. J. Feng, Y. L. Tan and Z. J. Tan, Predicting 3D structure and stability of RNA pseudoknots in monovalent and divalent ion solutions, *PLoS Comput. Biol.*, 2018, **14**, e1006222.

[S2] L. Z. Sun, J. L. Qian, P. Cai, H. X. Hu, X. Xu and M. B. Luo, Mg^{2+} effects on the single-stranded DNA conformations and nanopore translocation dynamics, *Polymer*, 2022, **250**, 124895.

[S3] D. M. Hinckley, G. S. Freeman, J. K. Whitmer and J. J. de Pablo, An experimentally-informed coarse-grained 3-site-per-nucleotide model of DNA: structure, thermodynamics, and dynamics of hybridization, *J. Chem. Phys.*, 2013, **139**, 144903.

[S4] D. Zhang and S. J. Chen, IsRNA: an iterative simulated reference state approach to modeling correlated interactions in RNA folding, *J. Chem. Theory Comput.*, 2018, **14**, 2230–2239.

[S5] G. S. Manning, The molecular theory of polyelectrolyte solutions with applications to the electrostatic properties of polynucleotides, *Q. Rev. Biophys.*, 1978, **11**, 179–246.

[S6] N. A. Denesyuk and D. Thirumalai, Coarse-grained model for predicting RNA folding thermodynamics, *J. Phys. Chem. B*, 2013, **117**, 4901–4911.

[S7] D. Chakraborty, N. Hori and D. Thirumalai, Sequence-dependent three interaction site model for single- and double-stranded DNA, *J. Chem. Theory Comput.*, 2018, **14**, 3763–3779.